Separate Surface and Bulk Topological Anderson Localization Transitions in Disordered Axion Insulators

Cormac Grindall,[1,*] Alexander C. Tyner,[2,3,*] Ang-Kun Wu,[1,4] Taylor L. Hughes,[5] and J. H. Pixley[1,6]
[1]Department of Physics and Astronomy, Center for Materials Theory, Rutgers University, Piscataway, New Jersey 08854, USA
[2]Nordita, KTH Royal Institute of Technology and Stockholm University, 106 91 Stockholm, Sweden
[3]Department of Physics, University of Connecticut, Storrs, Connecticut 06269, USA
[4]Theoretical Division, T-4, Los Alamos National Laboratory (LANL), Los Alamos, New Mexico 87545, USA
[5]Department of Physics and Institute for Condensed Matter Theory, University of Illinois at Urbana-Champaign, Urbana, Illinois 61801, USA
[6]Center for Computational Quantum Physics, Flatiron Institute, 162 5th Avenue, New York, New York 10010, USA

(Received 31 March 2025; revised 5 August 2025; accepted 3 November 2025; published 25 November 2025; corrected 5 November 2026)

In topological phases of matter for which the bulk and boundary support distinct electronic gaps, there exists the possibility of decoupled mobility gaps in the presence of disorder. This is in analogy with the well-studied problem of realizing separate or concomitant bulk-boundary criticality in conventional Landau theory. Using a three-dimensional axion insulator having clean, gapped surfaces with $e^2/2h$ quantized Hall conductance, we show that the bulk and surface mobility gap evolve differently in the presence of disorder. The decoupling of the bulk and surface topology yields a regime that realizes a two-dimensional, unquantized anomalous Hall metal in the Gaussian unitary ensemble on each surface, which shares some spectral and response properties akin to the surface states of a conventional 3D topological insulator. The generality of these results, as well as extensions to other insulators and superconductors, is discussed.

DOI: 10.1103/v7x8-ghfy

Introduction—The resilience of topological insulators (TIs) to disorder [1–16], and the utility of their similarly robust gapless surface states, have made these systems of paramount importance for potential technological applications [17–28]. However, the discovery of axion insulators and higher-order topological insulators, which have gapped bulk and *gapped* boundary excitations, has opened the door to a richer landscape of possible physical phenomena and has extended our understanding of topological bulk-boundary correspondences [29–47].

The dichotomy between TIs with gapped or gapless surfaces is brought into sharp focus in the context of disordered systems. Conventionally, properties of a disordered TI are controlled by a bulk mobility gap [5,10,48–68], which can be closed for sufficiently large disorder strengths. However, for TIs having gapped boundaries, the separate bulk and surface insulating gaps allow distinct mobility gaps and transitions. For bulk higher-order topological transitions in the presence of disorder, the dimensionally reduced surface states smear the transition, creating an intervening metallic phase separating topological and trivial insulating phases [69]. This mechanism is distinct from the nonperturbative effects that also smear the transition for $\mathbb{Z}_2$ insulators [70]. Upon opening the boundaries, prior work has shown that this allows for the boundary mobility gap to close, while the bulk mobility gap remains open, producing a (de)localization transition on only the surface [46,49–69,71,72]. This presents the possibility of realizing an Anderson localization analog of the well-studied question of separate versus concomitant bulk-boundary criticality in conventional Landau theory [73–77], a topic of recent interest. Nonetheless, an understanding of the universality classes of the separate surface and bulk transitions has been lacking. It is also important to understand and provide a clear description (or "labeling") of the intermediate phase with a gapless surface, but gapped higher-order topological bulk [Fig. 1(a)], a concept that has remained vague in the literature.

To be concrete, in the following we focus on the fate of axion insulators in the presence of disorder, which is of theoretical, experimental, and practical interest [69,72,99,100]. Generically, a clean axion insulator having broken time-reversal symmetry will have gapped surfaces that exhibit a quantized surface Hall conductance of opposite sign and equal magnitude $e^2/(2h)$—i.e., half the value of the conventional integer quantum Hall effect.

[*]These authors contributed equally to this work.

Published by the American Physical Society under the terms of the Creative Commons Attribution 4.0 International license. Further distribution of this work must maintain attribution to the author(s) and the published article's title, journal citation, and DOI. Funded by Bibsam.

However, transport measurements of the Hall conductivity using a standard Hall bar geometry will necessarily yield zero due to the two surfaces canceling. In the presence of weak disorder, the surface mobility gap will remain open [99], but stronger disorder may close the surface mobility gap while leaving the bulk mobility gap open. Here, we find that upon increasing the strength of disorder beyond the critical value necessary for closure of the surface mobility gap, the surface Hall conductance (on the opposing surfaces) decreases continuously from a magnitude of $e^2/(2h)$ to zero. This is different from the discontinuous jump in the Chern number that has been observed in isolated 2D quantum Hall layers. In contrast, to clearly observe the vanishing of surface Hall conductivity due to disorder, measurements of an individual surface are essential, and we expect they can be observed via measurements of the Kerr rotation [101]. Additionally, recent experiments [101–103] suggest that this may be measurable (though not fully quantized) in DC transport measurements of semimagnetic insulators for which a single-surface Hall conductivity of $0.52 \pm 0.03 e^2/h$ has been reported in the clean limit [102].

To this end, we study an axion insulator [1–16,99,104] in the presence of short-ranged quenched disorder. When the surface gap is smaller than the bulk gap in the clean limit, we demonstrate distinct bulk and surface critical points that are in agreement with the 3D Gaussian unitary ensemble (GUE) Anderson localization transition, and the 2D integer quantum Hall (IQH) plateau transition universality classes, respectively. Qualitatively, this suggests two critical disorder strengths at weak disorder: the first is on the scale of the surface mobility gap, and the second is on the order of the bulk mobility gap. In contrast, at large disorder (on the order of the bandwidth of the clean model), the surface and bulk will localize together. In particular, we find that the surface critical point separates an insulating phase with $1/2$-quantized Hall conductance and a 2D GUE metallic phase having a nonquantized surface Hall conductivity (but finite mobility gap in the 3D bulk), which is monotonically decreasing in magnitude with increasing disorder strength [see Figs. 1(a) and 1(c)]. In this phase, where the surface (bulk) mobility gap is closed (open) [see the region of the phase diagram between the teal and red lines in Fig. 1(a)], the disorder averaged surface spectral function reveals a characteristic Dirac spectrum [see upper left inset of Fig. 1(a)]. Furthermore, we put forth a protocol for determining the topological nature of the surface before *and* after closure of the mobility gap by proximity-coupling an s-wave superconductor. The gapless surface states reveal properties consistent with the conventional Fu-Kane mechanism [105] for each disorder sample—i.e., we find Majorana zero modes (MZMs) where vortex lines intersect the proximitized surface.

Model—We consider the tight-binding model of an antiferromagnetic (AFM) TI on a simple cubic lattice [99]

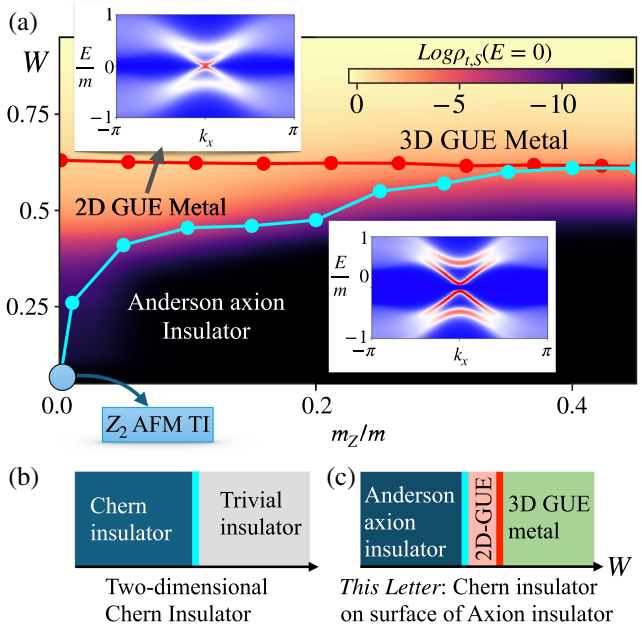


FIG. 1. Phase diagram at the band center of a disordered 3D axion insulator: (a) Surface typical density of states fixing $E/m = 0$ as a function of disorder strength W and staggered Zeeman field m_Z/m. Above the teal-colored phase boundary, the surface mobility gap is closed, and the surface anomalous Hall conductivity is no longer quantized to $\pm e^2/(2h)$. Above the red phase boundary, the bulk mobility gap is also closed, coinciding with a change in the bulk topology. The insets detail results of a disorder averaged surface spectral function for $m_Z/m = 0.1$: (right) prior to closure of the bulk and surface mobility gap ($W = 0.3$), and (left) after closure of the surface mobility gap ($W = 0.5$), revealing a massless Dirac cone. At large disorder strengths (of the order of the clean bandwidth), the surface and bulk localize concomitantly within the Gaussian unitary ensemble (GUE) universality class for $m_z > 0$ and the GSE universality class for $m_z = 0$ (see the Supplemental Material [78]). (b) Phase diagram at the band center for a disordered two-dimensional Chern insulator within the GUE class, displaying a closed mobility gap and critical states only at the topological phase transition point (see the Supplemental Material [78]) (c) Phase diagram at the band center for a half-quantized anomalous Hall surface of a 3D axion insulator that first transitions to a two-dimensional metallic phase having an unquantized anomalous Hall conductivity, and then to a three-dimensional metallic phase as disorder is increased.

in the presence of a quenched, short-range disorder potential. The disorder potential is sampled from a Gaussian distribution with zero mean and variance W^2, and hence W characterizes the strength of disorder. The strength of the staggered Zeeman field which gaps the z-surface states, m_z, is provided in units of the on-site orbital energies, m. Full details of the model are provided in Appendix A.

We note that the universal critical exponents we compute are independent of this choice of disorder distribution but nonuniversal details; e.g., the shape of the phase diagram will depend quantitatively upon it.

Bulk and surface delocalization transitions—A phase diagram in the presence of disorder and staggered Zeeman field m_Z is constructed by computing the typical density of states (TDOS). The TDOS involves computing the geometric mean of the local density of states which is not self-averaging, allowing extended and localized states to be distinguished in disordered systems. Identifying where the TDOS becomes finite in the thermodynamic limit is therefore a diagnostic of Anderson localization phase boundaries in any dimension [106–109]. Details of the TDOS computation as a function of energy, $\rho_t(E)$, are available in subsection "Typical density of states" of Appendix B.

We focus on the TDOS at the band center ($E = 0$), since the band structure is symmetric about zero energy in the clean limit, and upon disorder averaging, since the disorder potential is selected from a Gaussian distribution with zero mean (see the Supplemental Material for data away from the band center [78]). As shown in Fig. 2(a), the surface TDOS at the band center $\rho_t(E = 0)$ lifts off from zero well before the bulk does; at large enough disorder, $\rho_t(E = 0)$ is converged in expansion order and system size (see the Supplemental Material for data including smaller sizes [78]). Near the transitions, however, there is a large, finite KPM expansion order correction that we take into account using the scaling theory of Anderson localization [110].

To extract the bulk and surface mobility edges, we fit the data in Fig. 2(a) for W larger than the critical values to a power-law vanishing TDOS,

$$\rho_{t,j}(E = 0) \sim |W - W_{c,j}|^{\beta_j} \tag{1}$$

(where $j = S, B$ denotes surface and bulk), to determine $W_{c,S}$ and $W_{c,B}$ as a function of N_c; the fits to the largest N_c are shown as black lines in Fig. 2(a) and are shown on a log-log scale in the Supplemental Material [78]. The values of $W_{c,j}$ are subsequently extrapolated to the limit $N_c \to \infty$ through a linear fit as a function of $1/N_c$, shown in the upper panel of Fig. 2(b). This yields $W_{c,B} = 0.59 \pm 0.02$ and $W_{c,S} = 0.46 \pm 0.02$, clearly demonstrating that the surface localization transition precedes the bulk. We use this procedure to determine the phase diagram in Fig. 1(a) as we vary the strength of the disorder W and the staggered Zeeman field m_Z/m. For large values of m_Z/m, the surface gap becomes equivalent to the bulk gap in the clean limit, and the phase boundaries merge. For $m_Z \gg m$, the topological bulk gap will close, and the model will transition to a trivial insulator via a diffusive metal phase [69] (see the Supplemental Material [78]).

By extrapolating the fits for β_j (where $j = S, B$) shown in the lower panel of Fig. 2(b) to the limit $N_c \to \infty$, we find $\beta_B = 1.76 \pm 0.1$ for the bulk, and $\beta_S = 1.64 \pm 0.1$ for the surface for $m_Z/m = 0.1$. The value of $\beta_{j=S,B}$ is explored for additional values of m_Z/m in the Supplemental Material, yielding consistent results [78]. Utilizing the values of β and W_c, we fit $\rho_t(E = 0)$ at the band center to the scaling form in energy [111]

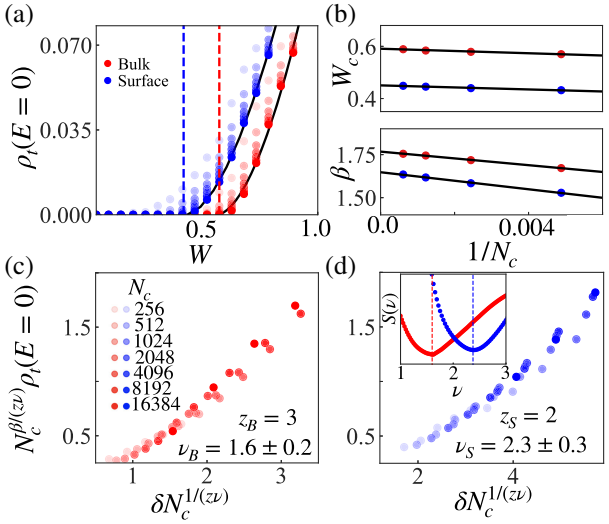


FIG. 2. Bulk and surface typical density of states: Fixing $m_Z/m = 0.1$, we vary W to pass through each phase of the model shown in Fig. 1. (a) Red points mark bulk typical density of states at at $E = 0$, and blue points mark surface typical density of states at the band center $E = 0$ as a function of KPM expansion order N_c and disorder strength W. Black lines are determined by fitting points to $\rho_t \sim |W - W_{c,j}|^{\beta_j}$, where $j = B, S$ for the bulk and surface, respectively. Insulator-to-metal transition points for the surface and bulk are marked by vertical dashed lines. (b) Fitting W_c and β as a function of $1/N_c$ for the surface and bulk to determine each quantity in the limit $N_c \to \infty$. (c) Data collapse of bulk typical density of states (TDOS), fixing $z = 3$ and utilizing values of β and W_c as determined from (b). The exponent ν_j is determined by the minimum of a similarity function $S(\nu_j)$ shown in the inset of (d). (d) Data collapse for surface TDOS, fixing $z = 2$ and determining ν using the similarity function.

$$\rho_{t,j}(E = 0) \sim N_c^{-\beta_j/(z_j\nu_j)} f\left(\delta_j N_c^{1/(\nu_j z_j)}\right), \tag{2}$$

where $\delta_j = |W - W_{c,j}|/W_{c,j}$ and $z_j = d_j$, fixing $z_B = 3$ and $z_S = 2$. The data are then collapsed by optimizing ν_j using a similarity function, $S_j(\nu)$, as shown in the inset of Fig. 2(d). We find $\nu_B = 1.6 \pm 0.2$ and $\nu_S = 2.3 \pm 0.3$ for the bulk and surface, respectively, as shown in Figs. 2(c) and 2(d).

Based purely on symmetry, the system falls under the GUE, since the Zeeman field breaks time-reversal symmetry. The values of ν_j determined through the finite size scaling analysis are generally in agreement with the expected values for a GUE Anderson localization transition in 3D at $W_{c,B}$ ($\nu_{3D} \approx 1.56$) and the 2D IQH plateau transition at $W_{c,S}$ ($\nu_{2D} \approx 2.25$) [112–115]. We find that for $W_{c,S} < W < W_{c,B}$, the mobility gap is closed; hence, the surface is a 2D GUE metal while the bulk is insulating. To provide further evidence of the GUE

metal phase, we performed detailed analysis of the level spacing statistics presented in the Supplemental Material [78]. At large disorder—i.e., when disorder is on the order of the clean bandwidth—there is no separation between surface and bulk localization, as they both have the same critical disorder strength (see the Supplemental Material [78]). Turning off the time-reversal symmetry breaking $m_Z = 0$ changes the bulk 3D localization to Gaussian symplectic ensemble (GSE) [12,13,15,78,116,117].

With this evidence in hand, one can ask if the surface critical point differs in any significant ways from the disorder induced topological phase transition in conventional Chern insulators as depicted in Fig. 1(b). First, our estimated value of $\beta_S \approx 1.6$ is much larger then what has been found at the IQH transition, $\beta = 0.58$ [114,118–121]. However, we can seek internal consistency through scaling, as the TDOS exponent can be related to the multifractal nature of the wave functions at the localization transition through the expression $\beta = \nu(\tilde{\alpha}_0 - d)$ [106], where $\tilde{\alpha}_0$ is a measure of the multifractal spectrum [110]. The obtained values of β_j and ν_j yield $\tilde{\alpha}_0^B = 4.0 \pm 0.3$ and $\tilde{\alpha}_0^S = 2.6 \pm 0.35$. We find that the obtained value for the bulk is in agreement with the expected value for the 3D unitary class [119], $\tilde{\alpha}_0^{3D} \approx 4.0$. The expected value for the 2D IQH transition, $\tilde{\alpha}_0^{2D} \approx 2.25$ [122], also lies within the margin of error for the obtained value of $\tilde{\alpha}_0^S$. Taken together, our analysis of the TDOS data demonstrates the existence of separate bulk and surface transitions and an extended parameter regime in which the disordered two-dimensional surface is a 2D GUE metal.

Surface spectrum and topological response—While we have demonstrated that the surface mobility gap is closed when $W > W_{c,S}$, we can gain more information by computing the surface resolved spectral function using KPM [123]. For a definition of this quantity see subsection "Surface spectral function" of Appendix B. The results are averaged over 100 disorder configurations, considering a system size $L = 60$ and $N_c = 2^{12}$. The results are shown in the inset of Fig. 1(a), which identifies clear regions showing characteristic gapped ($W < W_{c,S}$) and gapless ($W_{c,S} < W_{c,B}$) 2D surface Dirac cones.

While the surface spectral function in the 2D GUE metal regime indicates a gapless Dirac spectrum on average, it is important to understand the response phenomena of the surface and bulk as well. We first consider the topological response of the surface in the presence of disorder. To accomplish this, we compute the local Chern marker on the surface [124,125]; details of this computation are provided in subsection "Local Chern marker" of Appendix B. In the limit of weak disorder, the local Chern marker shows convergence to the quantized half-integer value in Fig. 3. Increasing the disorder strength beyond $W_{c,S}$, we observe a finite value that deviates from a half-integer. This is indicative of the surface being a GUE metal having a nonquantized anomalous Hall effect, even though the

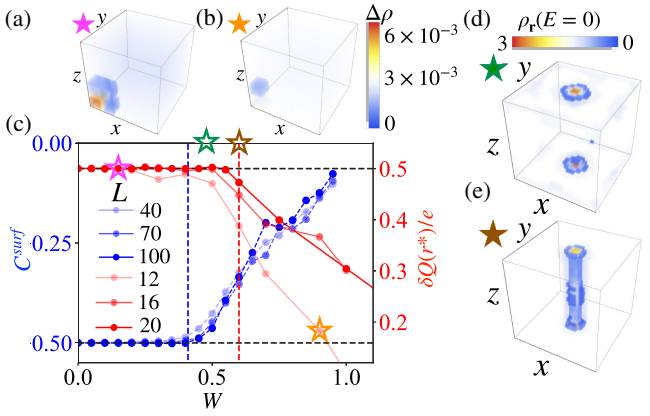


FIG. 3. Evolution of bulk and surface topology: (a),(b) Disorder-averaged, induced charge density within the first octant upon monopole insertion. The quantized monopole bound charge $\delta Q(\mathbf{r})$ is visible for (a) $W < W_{c,B}$, and absent for (b) $W > W_{c,B}$. (c) Induced charge on the monopole at the origin, computed using Eq. (B4) and exact diagonalization, within a radius $r* = L/4$ about the origin, where r is given in units of the linear system size $L = 20$ (red points). Surface Chern marker C^{surf} on the $\hat{z}$-surface computed using KPM as defined in Eq. (B3), averaged over 5000 disorder configurations fixing $N_c = 16384$ (blue points). The approximate values of disorder for the surface and bulk mobility gap closing are marked by blue and red dashed lines, respectively. (d),(e) Spatially resolved, zero-energy density of states of Eq. (B5), fixing $\mu = 0, m_Z/m = 0.1$ and $\delta_0 = 0.3$ averaged over 50 disorder configurations for (d) $W_{c,S} < W < W_{c,B}$ and (e) $W = W_{c,B}$. Colored stars are used to identify density plots with values of disorder strength in (c).

average surface spectra indicates a gapless Dirac cone. We confirm the Hall conductance by computing the charge bound to a flux tube passing through the top z-surface. We find that such a flux tube binds a charge on the surface in correspondence with the quantized (unquantized) Chern marker for $W < W_{c,S}$ ($W > W_{c,S}$) (see the Supplemental Material for details [78]). By comparison, we can probe the bulk response using the Witten effect [126–131]. That is, we can determine the charge bound to a magnetic monopole inserted in the bulk, which is expected to obey $Q_M = (e\theta/2\pi)$, even in a disordered system.

To determine the charge bound to the monopole, we compute the induced charge density at half-filling, $\Delta\rho(\mathbf{r}_i)$, via the procedure detailed in subsection "Witten effect" of Appendix B. The induced charge on the monopole, $\delta Q(\mathbf{r})$, is then obtained by integrating $\Delta\rho(\mathbf{r}_i)$ inside a spherical surface of radius R (all lengths are specified relative to the lattice spacing), centered at the monopole. As shown in Fig. 3(a), the charge is sharply localized on the monopole and, up to finite size effects, the bound charge is quantized to $Q_M = (e/2)$ all the way to the bulk transition—i.e., even when the surface mobility gap is closed. Hence, we find a robust value $\theta = \pi$ in the bulk for the entire region, $W < W_{c,B}$. After the bulk transition, there can still be charge density near the location of the monopole, but it is

not quantized and depends on the details of the inhomogeneity induced by the disorder.

In addition to the electromagnetic response, we can probe the bulk and surface topology by proximity-coupling the system to an s-wave superconductor, as in the work of Fu and Kane [105]. In the clean limit, if the proximity-induced superconducting gap dominates over the magnetic surface gap, then vortices that intersect the surface will bind MZMs. Hence, in the regime of disorder where the surface gap has closed but the bulk gap remains open, $W_{c,S}(m_z) < W < W_{c,B}$, we expect that even weak superconductivity should be able to open a surface gap to exhibit the Fu-Kane phenomenology. To model this scenario, we use a Bogoliubov–de Gennes (BdG) Hamiltonian, the details of which are provided in subsection "Fu-Kane effect" of Appendix B. To generate MZMs, we can follow the procedure in Refs. [132–134] to insert a vortex line along the z-axis (see the Supplemental Material [78]). The results are shown in Fig. 3(d), which reveal clear localized MZMs. Furthermore, we show that by tuning the chemical potential, μ, a vortex phase transition vanquishing the MZMs is observable, as expected from, e.g., Refs. [132,134] (see the Supplemental Material [78]).

Interestingly, in Fig. 3(e), we show that the vortex phase transition can also be accessed by tuning the disorder strength while keeping the chemical potential fixed. Using the Lanczos algorithm [135] at fixed μ and $m_z/m = 0.1$, we average the spatial localization of the zero-energy states for 50 disorder configurations, with the results shown in Figs. 3(d) and 3(e). For $W_{c,S} < W < W_{c,B}$, we clearly observe localized MZMs, while when $W = W_{c,B}$, the delocalization transition and hybridization across the vortex line is visible. Hence, we find that the Fu-Kane MZMs are apparent for $W > W_{c,S}$ but are removed by the bulk transition when $W > W_{c,B}$.

Discussion and outlook—We have shown that the introduction of disorder in an axion insulator supporting a gapped topological bulk and gapped topological surface leads to the decoupling of the surface and bulk mobility gaps. This decoupling gives rise to a novel phase in which each surface hosts a single gapless Dirac cone (with opposite chiralities on the two surfaces) within the GUE, a situation that has previously been found at the IQH plateau transition (for a single value of disorder strength, not over an extended range of disorder strength), which suggests the presence of a topological Θ term in the field-theoretic description of this system.

There could also be a scenario where a critical phase, not a critical point, exists where the multifractal dimensions of the wave functions would remain "pinned" to the 2D IQH transition values for a range of disorder strengths. However, our data are inconsistent with this scenario (see the Supplemental Material [78]) as the surface density of states converges to a finite value in the thermodynamic limit—i.e., it does not vanish in a power-law fashion as it would at the IQH transition.

We expect this Letter to have widespread consequences, as the class of axion insulators includes magnetic topological insulators [129,136] beyond the AFM case we investigated. Many higher-order topological insulators (HOTIs) have been shown to fall into this class [35–37], providing a broad range of known systems that can realize the physics described in this Letter. The strategy for diagnosing topology before *and* after closure of the surface mobility gap is also general and can be applied to understand such HOTIs.

Acknowledgments—We thank Matthew Foster and David Huse for insightful discussions, as well as David Vanderbilt and Justin Wilson for discussions and collaborations on related work. This work is partially supported by NSF Career Grant No. DMR-1941569 and the Alfred P. Sloan Foundation through a Sloan Research Fellowship (C. G., A.-K. W., J. H. P.). Part of this work was performed in part at the Aspen Center for Physics, which is supported by National Science Foundation Grant No. PHY-2210452 (A. T., J. H. P.) A. T. acknowledges the hospitality of the Center for Materials Theory at Rutgers University. NORDITA is supported in part by NordForsk. A portion of this research was done using services provided by the OSG Consortium [137–140], which is supported by National Science Foundation Awards No. 2030508 and No. 1836650. The authors acknowledge the Office of Advanced Research Computing (OARC) at Rutgers, The State University of New Jersey, for providing access to the Amarel cluster and associated research computing resources that have contributed to the results reported here. A portion of the computations were enabled by resources provided by the National Academic Infrastructure for Supercomputing in Sweden (NAISS), partially funded by the Swedish Research Council through Grant Agreement No. 2022-06725. A.-K. W. is partially supported by the U.S. Department of Energy (DOE) National Nuclear Security Administration under Contract No. 89233218CNA000001 through the Laboratory Directed Research and Development Program, and this research was performed, in part, at the Center for Integrated Nanotechnologies, an Office of Science User Facility operated for the DOE Office of Science, under user Proposals No. 2018BU0010 and No. 2018BU0083. T. L. H. thanks the U.S. Army Research Laboratory and the U.S. Army Research Office under Grant No. W911NF2020166 for support.

Data availability—The data that support the findings of this article are not publicly available upon publication, because it is not technically feasible and/or the cost of preparing, depositing, and hosting the data would be prohibitive within the terms of this research project. The data are available from the authors upon reasonable request.

[1] C. L. Kane and E. J. Mele, Phys. Rev. Lett. **95**, 146802 (2005).
[2] L. Fu and C. L. Kane, Phys. Rev. B **76**, 045302 (2007).
[3] B. A. Bernevig, T. L. Hughes, and S.-C. Zhang, Science **314**, 1757 (2006).
[4] X.-L. Qi, T. L. Hughes, and S.-C. Zhang, Phys. Rev. B **78**, 195424 (2008).
[5] C. Xu and J. E. Moore, Phys. Rev. B **73**, 045322 (2006).
[6] S. Ryu, C. Mudry, H. Obuse, and A. Furusaki, Phys. Rev. Lett. **99**, 116601 (2007).
[7] A. P. Schnyder, S. Ryu, A. Furusaki, and A. W. W. Ludwig, AIP Conf. Proc. **1134**, 10 (2009).
[8] R. Shindou and S. Murakami, Phys. Rev. B **79**, 045321 (2009).
[9] S. Ryu, A. P. Schnyder, A. Furusaki, and A. W. Ludwig, New J. Phys. **12**, 065010 (2010).
[10] M. Z. Hasan and C. L. Kane, Rev. Mod. Phys. **82**, 3045 (2010).
[11] G. Schubert, H. Fehske, L. Fritz, and M. Vojta, Phys. Rev. B **85**, 201105(R) (2012).
[12] B. Leung and E. Prodan, Phys. Rev. B **85**, 205136 (2012).
[13] K. Kobayashi, T. Ohtsuki, and K.-I. Imura, Phys. Rev. Lett. **110**, 236803 (2013).
[14] T. Morimoto and A. Furusaki, Phys. Rev. B **89**, 035117 (2014).
[15] H. Katsura and T. Koma, J. Math. Phys. (N.Y.) **57**, 021903 (2016).
[16] C.-K. Chiu, J. C. Y. Teo, A. P. Schnyder, and S. Ryu, Rev. Mod. Phys. **88**, 035005 (2016).
[17] J. C. Budich and E. J. Bergholtz, Phys. Rev. Lett. **125**, 180403 (2020).
[18] Z. F. Wang and F. Liu, Phys. Rev. Lett. **115**, 026803 (2015).
[19] L. Viti, D. Coquillat, A. Politano, K. A. Kokh, Z. S. Aliev, M. B. Babanly, O. E. Tereshchenko, W. Knap, E. V. Chulkov, and M. S. Vitiello, Nano Lett. **16**, 80 (2016).
[20] G. Konstantatos, Nat. Commun. **9**, 5266 (2018).
[21] N. Lang and H. P. Büchler, npj Quantum Inf. **3**, 47 (2017).
[22] M. J. Gilbert, Commun. Phys. **4**, 70 (2021).
[23] M. Wang, Q. Fu, L. Yan, W. Pi, G. Wang, Z. Zheng, and W. Luo, ACS Appl. Mater. Interfaces **11**, 47868 (2019).
[24] L. Z. Tan and A. M. Rappe, Phys. Rev. Lett. **116**, 237402 (2016).
[25] C. Nayak, S. H. Simon, A. Stern, M. Freedman, and S. Das Sarma, Rev. Mod. Phys. **80**, 1083 (2008).
[26] J. D. Sau, R. M. Lutchyn, S. Tewari, and S. Das Sarma, Phys. Rev. Lett. **104**, 040502 (2010).
[27] S. D. Sarma, M. Freedman, and C. Nayak, npj Quantum Inf. **1**, 1 (2015).
[28] M. Freedman, A. Kitaev, M. Larsen, and Z. Wang, Bull. Am. Math. Soc. **40**, 31 (2003).
[29] F. Tang, H. C. Po, A. Vishwanath, and X. Wan, Nat. Phys. **15**, 470 (2019).
[30] T. Zhang, Y. Jiang, Z. Song, H. Huang, Y. He, Z. Fang, H. Weng, and C. Fang, Nature (London) **566**, 475 (2019).
[31] M. Vergniory, L. Elcoro, C. Felser, N. Regnault, B. A. Bernevig, and Z. Wang, Nature (London) **566**, 480 (2019).
[32] F. Tang, H. C. Po, A. Vishwanath, and X. Wan, Nature (London) **566**, 486 (2019).
[33] Y. Xu, L. Elcoro, Z.-D. Song, B. J. Wieder, M. Vergniory, N. Regnault, Y. Chen, C. Felser, and B. A. Bernevig, Nature (London) **586**, 702 (2020).
[34] F. Schindler, Z. Wang, M. G. Vergniory, A. M. Cook, A. Murani, S. Sengupta, A. Y. Kasumov, R. Deblock, S. Jeon, I. Drozdov *et al.*, Nat. Phys. **14**, 918 (2018).
[35] F. Schindler, A. M. Cook, M. G. Vergniory, Z. Wang, S. S. P. Parkin, B. A. Bernevig, and T. Neupert, Sci. Adv. **4**, eaat0346 (2018).
[36] W. A. Benalcazar, B. A. Bernevig, and T. L. Hughes, Science **357**, 61 (2017).
[37] W. A. Benalcazar, T. Li, and T. L. Hughes, Phys. Rev. B **99**, 245151 (2019).
[38] E. Khalaf, Phys. Rev. B **97**, 205136 (2018).
[39] D. Călugăru, V. Juričić, and B. Roy, Phys. Rev. B **99**, 041301(R) (2019).
[40] B. J. Wieder, Z. Wang, J. Cano, X. Dai, L. M. Schoop, B. Bradlyn, and B. A. Bernevig, Nat. Commun. **11**, 627 (2020).
[41] M. J. Park, Y. Kim, G. Y. Cho, and S. B. Lee, Phys. Rev. Lett. **123**, 216803 (2019).
[42] B. Xie, H.-X. Wang, X. Zhang, P. Zhan, J.-H. Jiang, M. Lu, and Y. Chen, Nat. Rev. Phys. **3**, 520 (2021).
[43] L. Trifunovic and P. W. Brouwer, Phys. Rev. X **9**, 011012 (2019).
[44] Sayed Ali Akbar Ghorashi, T. Li, and T. L. Hughes, Phys. Rev. Lett. **125**, 266804 (2020).
[45] E. Khalaf, H. C. Po, A. Vishwanath, and H. Watanabe, Phys. Rev. X **8**, 031070 (2018).
[46] E. Khalaf, W. A. Benalcazar, T. L. Hughes, and R. Queiroz, Phys. Rev. Res. **3**, 013239 (2021).
[47] W. A. Benalcazar and A. Cerjan, Phys. Rev. Lett. **128**, 127601 (2022).
[48] X.-L. Qi and S.-C. Zhang, Rev. Mod. Phys. **83**, 1057 (2011).
[49] C.-A. Li, B. Fu, Z.-A. Hu, J. Li, and S.-Q. Shen, Phys. Rev. Lett. **125**, 166801 (2020).
[50] Y.-S. Hu, Y.-R. Ding, J. Zhang, Z.-Q. Zhang, and C.-Z. Chen, Phys. Rev. B **104**, 094201 (2021).
[51] C. Wang and X. R. Wang, Phys. Rev. Res. **2**, 033521 (2020).
[52] J.-H. Wang, Y.-B. Yang, N. Dai, and Y. Xu, Phys. Rev. Lett. **126**, 206404 (2021).
[53] C. Wang and X. R. Wang, Phys. Rev. B **103**, 115118 (2021).
[54] Y. Shen, Z. Li, Q. Niu, and Z. Qiao, Phys. Rev. B **109**, 035303 (2024).
[55] Y.-L. Tao, J.-H. Wang, and Y. Xu, SciPost Phys. **15**, 193 (2023).
[56] Y.-R. Ding, D.-H. Xu, and C.-Z. Chen, arXiv:2401.13443.
[57] Y.-B. Yang, J.-H. Wang, K. Li, and Y. Xu, J. Phys. Condens. Matter **36**, 283002 (2024).
[58] Z. Su, Y. Kang, B. Zhang, Z. Zhang, and H. Jiang, Chin. Phys. B **28**, 117301 (2019).
[59] A. Agarwala, V. Juričić, and B. Roy, Phys. Rev. Res. **2**, 012067(R) (2020).
[60] J.-H. Wang, Y.-B. Yang, N. Dai, and Y. Xu, Phys. Rev. Lett. **126**, 206404 (2021).
[61] T. Peng, C.-B. Hua, R. Chen, Z.-R. Liu, H.-M. Huang, and B. Zhou, Phys. Rev. B **106**, 125310 (2022).

[62] N. Okuma, M. Sato, and K. Shiozaki, Phys. Rev. B **99**, 085127 (2019).
[63] J. Yi and C. Q. Chen, New J. Phys. **26**, 063004 (2024).
[64] T. Nag, V. Juričić, and B. Roy, Phys. Rev. Res. **1**, 032045 (R) (2019).
[65] B. Roy and V. Juričić, Phys. Rev. Res. **3**, 033107 (2021).
[66] A. L. Szabó and B. Roy, Phys. Rev. Res. **2**, 043197 (2020).
[67] S. Manna, S. Nandy, and B. Roy, Phys. Rev. B **105**, L201301 (2022).
[68] M. Li, D. Zhirihin, M. Gorlach, X. Ni, D. Filonov, A. Slobozhanyuk, A. Alù, and A. B. Khanikaev, Nat. Photonics **14**, 89 (2020).
[69] Z.-D. Song, B. Lian, R. Queiroz, R. Ilan, B. A. Bernevig, and A. Stern, Phys. Rev. Lett. **127**, 016602 (2021).
[70] Y. Fu, J. H. Wilson, D. A. Huse, and J. H. Pixley, Phys. Rev. B **109**, 205106 (2024).
[71] J. Claes and T. L. Hughes, Phys. Rev. B **102**, 100203(R) (2020).
[72] H. Li, H. Jiang, C.-Z. Chen, and X. C. Xie, Phys. Rev. Lett. **126**, 156601 (2021).
[73] M. E. Fisher and A. E. Ferdinand, Phys. Rev. Lett. **19**, 169 (1967).
[74] H. W. Diehl and S. Dietrich, Phys. Rev. B **24**, 2878 (1981).
[75] H. W. Diehl, *Phase Transition and Critical Phenomena* (Academic Press, London, 1986), Vol. 10, pp. 75–267.
[76] H. W. Diehl, Int. J. Mod. Phys. B **11**, 3503 (1997).
[77] M. A. Metlitski, SciPost Phys. **12**, 131 (2022).
[78] See Supplemental Material at http://link.aps.org/supplemental/10.1103/v7x8-ghfy for more details, which includes Refs. [79–98].
[79] S. Coh and D. Vanderbilt, Phys. Rev. Lett. **102**, 107603 (2009).
[80] R. Yu, X. L. Qi, A. Bernevig, Z. Fang, and X. Dai, Phys. Rev. B **84**, 075119 (2011).
[81] A. A. Soluyanov and D. Vanderbilt, Phys. Rev. B **83**, 235401 (2011).
[82] A. Alexandradinata, X. Dai, and B. A. Bernevig, Phys. Rev. B **89**, 155114 (2014).
[83] M. Taherinejad, K. F. Garrity, and D. Vanderbilt, Phys. Rev. B **89**, 115102 (2014).
[84] D. Gresch, G. Autès, O. V. Yazyev, M. Troyer, D. Vanderbilt, B. A. Bernevig, and A. A. Soluyanov, Phys. Rev. B **95**, 075146 (2017).
[85] A. Bouhon, A. M. Black-Schaffer, and R.-J. Slager, Phys. Rev. B **100**, 195135 (2019).
[86] B. Bradlyn, Z. Wang, J. Cano, and B. A. Bernevig, Phys. Rev. B **99**, 045140 (2019).
[87] E. Prodan, T. L. Hughes, and B. A. Bernevig, Phys. Rev. Lett. **105**, 115501 (2010).
[88] A. Chandran, V. Khemani, and S. L. Sondhi, Phys. Rev. Lett. **113**, 060501 (2014).
[89] H. Yao and X.-L. Qi, Phys. Rev. Lett. **105**, 080501 (2010).
[90] X.-L. Qi, H. Katsura, and A. W. W. Ludwig, Phys. Rev. Lett. **108**, 196402 (2012).
[91] L. Fidkowski, Phys. Rev. Lett. **104**, 130502 (2010).
[92] F. Pollmann, A. M. Turner, E. Berg, and M. Oshikawa, Phys. Rev. B **81**, 064439 (2010).
[93] W. Buijsman, V. Cheianov, and V. Gritsev, Phys. Rev. Lett. **122**, 180601 (2019).
[94] V. Juričić, A. Mesaros, R.-J. Slager, and J. Zaanen, Phys. Rev. Lett. **108**, 106403 (2012).
[95] A. Mesaros, R.-J. Slager, J. Zaanen, and V. Juričić, Nucl. Phys. **B867**, 977 (2013).
[96] E. Prodan, Phys. Rev. B **80**, 125327 (2009).
[97] Y. Xue and E. Prodan, Phys. Rev. B **87**, 115141 (2013).
[98] M. Moreno-Gonzalez, J. Dieplinger, and A. Altland, Ann. Phys. (Amsterdam) **456**, 169258 (2023).
[99] N. Varnava, J. H. Wilson, J. Pixley, and D. Vanderbilt, Nat. Commun. **12**, 3998 (2021).
[100] J. Pixley, N. Varnava, D. Vanderbilt, and J. Wilson, Controlling a quantum point junction on the surface of an antiferromagnetic topological insulator, U.S. Patent No. 12,315,658 (2025).
[101] M. Mogi, Y. Okamura, M. Kawamura, R. Yoshimi, K. Yasuda, A. Tsukazaki, K. Takahashi, T. Morimoto, N. Nagaosa, M. Kawasaki *et al.*, Nat. Phys. **18**, 390 (2022).
[102] R. Jain, M. Roddy, V. Gupta, B. Huang, H. M. Sayeed, H. F. Alnaser, A. Vashist, K. Watanabe, T. Taniguchi, V. V. Deshpande *et al.*, arXiv:2412.05380.
[103] D. Xiao, J. Hu, B. Wang, H. Zhou *et al.*, Res. Square (2025), 10.21203/rs.3.rs-7021873/v1.
[104] R. S. K. Mong, A. M. Essin, and J. E. Moore, Phys. Rev. B **81**, 245209 (2010).
[105] L. Fu and C. L. Kane, Phys. Rev. Lett. **100**, 096407 (2008).
[106] M. Janssen, Phys. Rep. **295**, 1 (1998).
[107] V. Dobrosavljević, A. Pastor, and B. Nikolić, Europhys. Lett. **62**, 76 (2003).
[108] A. Weiße, G. Wellein, A. Alvermann, and H. Fehske, Rev. Mod. Phys. **78**, 275 (2006).
[109] J. H. Pixley, P. Goswami, and S. Das Sarma, Phys. Rev. Lett. **115**, 076601 (2015).
[110] F. Evers and A. D. Mirlin, Rev. Mod. Phys. **80**, 1355 (2008).
[111] J. H. Pixley, D. A. Huse, and S. Das Sarma, Phys. Rev. B **94**, 121107(R) (2016).
[112] K. Slevin and T. Ohtsuki, Phys. Rev. Lett. **82**, 382 (1999).
[113] J. Brndiar and P. Markoš, Phys. Rev. B **74**, 153103 (2006).
[114] K. Slevin and T. Ohtsuki, Phys. Rev. B **80**, 041304(R) (2009).
[115] A. Rodriguez, L. J. Vasquez, K. Slevin, and R. A. Römer, Phys. Rev. B **84**, 134209 (2011).
[116] T. Kawarabayashi, T. Ohtsuki, K. Slevin, and Y. Ono, Phys. Rev. Lett. **77**, 3593 (1996).
[117] E. Prodan, J. Phys. A **44**, 113001 (2011).
[118] M. Amado, A. V. Malyshev, A. Sedrakyan, and F. Domínguez-Adame, Phys. Rev. Lett. **107**, 066402 (2011).
[119] L. Ujfalusi and I. Varga, Phys. Rev. B **91**, 184206 (2015).
[120] B. Sbierski, E. J. Dresselhaus, J. E. Moore, and I. A. Gruzberg, Phys. Rev. Lett. **126**, 076801 (2021).
[121] M. Puschmann, P. Cain, M. Schreiber, and T. Vojta, Phys. Rev. B **99**, 121301(R) (2019).
[122] F. Evers, A. Mildenberger, and A. D. Mirlin, Phys. Rev. Lett. **101**, 116803 (2008).
[123] J. H. Wilson, J. H. Pixley, D. A. Huse, G. Refael, and S. Das Sarma, Phys. Rev. B **97**, 235108 (2018).
[124] R. Bianco and R. Resta, Phys. Rev. B **84**, 241106(R) (2011).
[125] M. D. Caio, G. Möller, N. R. Cooper, and M. Bhaseen, Nat. Phys. **15**, 257 (2019).

[126] E. Witten, Phys. Lett. B **86**, 283 (1979).
[127] H. Yamagishi, Phys. Rev. D **27**, 2383 (1983).
[128] H. Yamagishi, Phys. Rev. D **28**, 977 (1983).
[129] G. Rosenberg and M. Franz, Phys. Rev. B **82**, 035105 (2010).
[130] Y.-Y. Zhao and S.-Q. Shen, arXiv:1208.3027.
[131] A. C. Tyner and P. Goswami, arXiv:2206.10636.
[132] P. Hosur, P. Ghaemi, R. S. K. Mong, and A. Vishwanath, Phys. Rev. Lett. **107**, 097001 (2011).
[133] C.-K. Chiu, M. J. Gilbert, and T. L. Hughes, Phys. Rev. B **84**, 144507 (2011).
[134] Sayed Ali Akbar Ghorashi, T. L. Hughes, and E. Rossi, Phys. Rev. Lett. **125**, 037001 (2020).
[135] C. Lanczos, J. Res. Natl. Bur. Stand. **45**, 255 (1950).
[136] G. Rosenberg, H.-M. Guo, and M. Franz, Phys. Rev. B **82**, 041104(R) (2010).
[137] R. Pordes, D. Petravick, B. Kramer, D. Olson, M. Livny, A. Roy, P. Avery, K. Blackburn, T. Wenaus, F. Wurthwein *et al.*, J. Phys. Conf. Ser. **78**, 012057 (2007).
[138] I. Sfiligoi, D. C. Bradley, B. Holzman, P. Mhashilkar, S. Padhi, and F. Wurthwein, in *2009 WRI World Congress on Computer Science and Information Engineering, Los Angeles, CA, USA* (2009), pp. 428–432, 10.1109/CSIE.2009.950.
[139] OSG, OSG 344, 10.21231/906P-4D78 (2006).
[140] OSG, OSG 344, 10.21231/0KVZ-VE57 (2015).
[141] N. Varnava, I. Souza, and D. Vanderbilt, Phys. Rev. B **101**, 155130 (2020).
[142] A. M. Essin, J. E. Moore, and D. Vanderbilt, Phys. Rev. Lett. **102**, 146805 (2009).
[143] N. Varnava and D. Vanderbilt, Phys. Rev. B **98**, 245117 (2018).
[144] D. Varjas, M. Fruchart, A. R. Akhmerov, and P. M. Perez-Piskunow, Phys. Rev. Res. **2**, 013229 (2020).

Correction: The omission of a support statement in the Acknowledgments has been fixed.

End Matter

Appendix A: Model Hamiltonian—Throughout this Letter, we consider the tight-binding model of an antiferromagnetic (AFM) TI on a simple cubic lattice [99] in the presence of a quenched, short-range disorder potential,

$$H = H_0 + H_V, \tag{A1}$$

where $H_0 = m\sum_l c_l^\dagger \tau^z c_l + m_z \sum_l (-1)^{l_z} c_l^\dagger \sigma^z c_l + (t/2) \sum_{\langle l,l\prime\rangle} c_l^\dagger \tau^z c_{l\prime} + (-i\lambda/2)\sum_{\langle l,l\prime\rangle} c_l^\dagger \tau^x \hat{\mathbf{n}} u\prime \cdot \sigma c_{l\prime}$, and disorder is introduced as $H_V = \sum_l V(l) c_l^\dagger c_l$, where $\tau^{\mu=x,y,z}$ and $\sigma^{\mu=x,y,z}$ are Pauli matrices for the orbital and spin degrees of freedom. Sites on the cubic lattice are labeled by l, with $\sum_{\langle l,l'\rangle}$ denoting a sum over nearest neighbors and $\hat{\mathbf{n}}_{ll'}$ denoting the nearest-neighbor unit vector. The on-site orbital energies and staggered Zeeman field strength are determined by m and m_Z, respectively; t dictates the spin-independent hopping strength, and λ is the spin-dependent nearest-neighbor hopping strength. The potential $V(l)$ is sampled from a Gaussian distribution with zero mean and variance W^2.

When $m_Z = 0$, this model reduces to a time-reversal-invariant 3D topological insulator having a gapped bulk and a quantized axion angle, $\theta = \pi$ for $|t| < |m| < |3t|$, and $\theta = 0$ for $|m| > |3t|$ or $|m| < |t|$. In phases where $\theta = \pi$, the system will have gapless surface states consisting of an odd number of surface Dirac cones [4]. We focus on the parameter choice $(m, t, \lambda) = (1.0, -0.5, -0.6)$. For $m_Z \neq 0$, the staggered Zeeman field gaps the topological surface states on the z-surfaces, but the quantization of θ remains, yielding an axion insulator [141,142]. The insulating z-surfaces have a quantized half-integer anomalous Hall effect [143]. Unless stated otherwise, we focus on the case $m_Z/m = 0.1$ in the main text.

Appendix B: Probes of the disordered model—

Typical density of states: In this Letter, we utilize the typical density of states to determine the Anderson localization phase boundaries. We define the typical density of states (TDOS) through the local DOS via

$$\rho_t(E) = \exp\left(\frac{1}{4N_s}\sum_{i=1}^{N_s}\sum_{\sigma=1}^{2}\sum_{\tau=1}^{2}[\ln \rho_{i,\sigma,\tau}(E)]\right), \tag{B1}$$

where $[\ldots]$ denotes a disorder average, N_s indicates a small collection of random sites to improve the average ($N_s \ll L^3$), and the local DOS at site i for spin σ and orbital τ, is defined as $\rho_{i,\sigma,\tau}(E) = \sum_n |\langle n|i,\sigma,\tau\rangle|^2 \delta(E - E_n)$, where $|n\rangle$ and E_n denote an exact eigenstate and its eigenenergy, respectively.

When examining the surface DOS, the sum over i is restricted to values on the surface of the sample. We restrict sampling for the bulk DOS to the half of the system closest to the middle to avoid any boundary effects. For the computation of the TDOS, we average 5000 disorder configurations and use the kernel polynomial method (KPM) [108] to expand the action of any operator that is dependent on the Hamiltonian on an eigenstate, $|n\rangle$, in terms of Chebyshev polynomials to order N_c. This allows us to access a large linear system size of $L = 100$. The surface and bulk TDOS computed for the model at hand are displayed in Fig. 2. Further details of the KPM method are available in the Supplemental Material [78].

Surface spectral function: The surface resolved spectral function is defined as

$$A(\mathbf{k}_\perp, z; E) = \sum_n \sum_{\sigma,\tau} |\langle \mathbf{k}_\perp, z, \sigma, \tau | n\rangle|^2 \delta(E - E_n), \tag{B2}$$

where $\mathbf{k}_\perp = (k_x, k_y)$, and $|n\rangle$ and E_n denote the exact eigenstate and eigenenergy, respectively.

We are using a mixed momentum-position basis $|\mathbf{k}_\perp, z, \sigma, \tau\rangle = (1/\sqrt{L^2}) \sum_{x,y} e^{i(k_x x + k_y y)} c^\dagger_{x,y,z,\sigma,\tau}|0\rangle$ for spin component σ, orbital component τ, and we take $z = 0$ to be the sample surface. The results of computing the surface spectral function averaged over 100 disorder configurations for a system size $L = 60$ and KPM expansion order $N_c = 2^{12}$ are shown as insets in Fig. 1 for (top left) $W < W_{c,S}$ and (bottom right) $W_{c,s} < W < W_{c,B}$.

Local Chern marker: The local Chern marker [124,125] is computed as

$$C_l(x, y) = \frac{2\pi i}{|\mathcal{A}|} \sum_s \langle s|[\hat{P}_l \hat{x} \hat{P}_l, \hat{P}_l \hat{y} \hat{P}_l]|s\rangle, \tag{B3}$$

where $\mathcal{A}$ is a subsystem constructed of sites on the z-layer indexed by l, with $|\mathcal{A}|$ being its area, and s spans all the degrees of freedom in the subsystem. We compute the local Chern marker via KPM [144], and we use coarse grain across z-layers to determine the value on the surface (see Ref. [143] and the Supplemental Material for more details [78]). Results for computing the Chern marker as a function of disorder strength are shown in Fig. 3(c).

Witten effect: To determine the charge bound to an inserted monopole, we compute the charge density at half filling,

$$\rho_q(\mathbf{r}_i) = -e \sum_{n=0}^{2L^3} |\psi_{n,q}(\mathbf{r}_i)|^2, \tag{B4}$$

in the presence ($q = M$) and absence ($q = 0$) of the monopole. We use a north-pole gauge to simulate the monopole, as described in the Supplemental Material [78]. The induced charge on the monopole is then obtained by integrating $\Delta\rho(\mathbf{r}_i) = \rho_M(\mathbf{r}_i) - \rho_0(\mathbf{r}_i)$ inside a spherical surface of radius R (all lengths are specified relative to the lattice spacing), centered at the monopole. For our discrete system, we explicitly compute $\delta Q(R) = \sum_{|\mathbf{r}_i|<R} \Delta\rho(\mathbf{r}_i)$ for a system having open boundaries along all directions. The disorder-averaged induced charge density fixing $W < W_{c,B}$ and $W > W_{c,B}$ is shown in Figs. 3(a) and 3(b), respectively. The induced charge on the monopole as a function of system size and disorder strength is shown in Fig. 3(c).

Fu-Kane effect: To explore the effects of proximity coupling an s-wave superconductor in the main body, we analyze the Bogoliubov–de Gennes (BdG) Hamiltonian,

$$H^{BdG} = \begin{bmatrix} H - \mu & \Delta_0 \tau_0 \sigma_2 \\ (\Delta_0 \tau_0 \sigma_2)^\dagger & -H^* + \mu \end{bmatrix}. \tag{B5}$$

Here, H is defined in Eq. (A1), μ is the chemical potential, and Δ_0 is the s-wave pairing amplitude. The choice of s-wave pairing follows the reasoning given in Ref. [44]—namely, that for this choice the bulk remains gapped, as the chemical potential is varied in the clean limit, and it is the form of pairing explored for TIs in Ref. [132]. To generate Majorana zero modes and probe the topological character of the surface states, a vortex line is inserted along the z-axis following the procedure in Refs. [132–134].

The disorder-averaged, spatially resolved, zero-energy density of states fixing $\mu = 0$ and $\delta_0 = 0.3$ is shown in Figs. 3(d) and 3(e) for $W_{c,S} < W < W_{c,B}$ and $W = W_{c,B}$, respectively. For $W_{c,S} < W < W_{c,B}$ [Fig. 3(d)], two Majorana zero modes are found at the ends of the vortex line. When $W = W_{c,B}$ [Fig. 3(e)], we observe a vortex phase transition in which the Majorana zero modes are vanquished.